High-contrast laser acceleration of relativistic electrons in solid cone-wire targets

D. P. Higginson,[1,2] A. Link,[2] H. Sawada,[1,3] S. C. Wilks,[2] T. Bartal,[1,2] S. Chawla,[1,2] C. D. Chen,[2] K. A. Flippo,[4] L. C. Jarrott,[1,2] M. H. Key,[2] H. S. McLean,[2] P. K. Patel,[2] F. Pérez,[2,5] M. S. Wei,[1,6] and F. N. Beg[1]

[1]*University of California-San Diego, La Jolla, California 92093, USA*

[2]*Lawrence Livermore National Laboratory, Livermore, California 94440, USA*

[3]*Department of Physics, University of Nevada, Reno, Nevada 89557, USA*

[4]*Los Alamos National Laboratory, Los Alamos, New Mexico 87545, USA*

[5]*Laboratoire pour l'Utilisation des Lasers Intenses, UMR 7605 CNRS-CEA-École Polytechnique-Université Paris VI, 91128 Palaiseau, France*

[6]*General Atomics, San Diego, California 92186, USA*

(Received 14 June 2013; revised manuscript received 24 November 2015; published 31 December 2015)

The consequences of small scale-length precursor plasmas on high-intensity laser-driven relativistic electrons are studied via experiments and simulations. Longer scale-length plasmas are shown to dramatically increase the efficiency of electron acceleration, yet, if too long, they reduce the coupling of these electrons into the solid target. Evidence for the existence of an optimal plasma scale-length is presented and estimated to be from 1 to 5 μm. Experiments on the Trident laser ($I = 5 \times 10^{19}$ W/cm^2) diagnosed via Kα emission from Cu wires attached to Au cones are quantitively reproduced using 2D particle-in-cell simulations that capture the full temporal and spatial scale of the nonlinear laser interaction and electron transport. The simulations indicate that 32% $\pm$ 8% (6.5% $\pm$ 2%) of the laser energy is coupled into electrons of all energies (1–3 MeV) reaching the inner cone tip and that, with an optimized scale-length, this could increase to 35% (9%).

DOI: 10.1103/PhysRevE.92.063112 PACS number(s): 52.38.Kd, 52.38.Dx, 52.38.Hb, 52.57.Kk

Optimizing the total number, energy, angular divergence, and subsequent coupling of relativistic electrons into solid-density targets is of interest to many fields for the purpose of proton acceleration [1–5], isochoric heating to form warm-dense or high-energy-density matter states [6–8], positron creation [9], x-ray source generation for backlighter diagnostics [10], and the fast ignition (FI) approach to inertial confinement fusion [11]. In order to accelerate electrons to relativistic energies [12], lasers must be high-intensity ($>10^{18}$ W/cm^2) and therefore if even a small portion of the laser pulse reaches the target prior to the peak of the pulse it will have high enough intensity ($>10^{11}$ W/cm^2) to ionize matter and create a plasma. In standard "low-contrast" laser systems there is often a few millijoules of energy that arrives over a period of a few nanoseconds prior to the peak of the pulse, and this creates a low-density plasma (known as preplasma) often extending hundreds of microns, and with which the laser interacts before it reaches the initial target surface. Previous studies have shown that this long preplasma can initiate and grow nonlinear instabilities such as relativistic self-focusing, filamentation, and hole-boring [13–15]; effects which are are imprinted onto the accelerated electrons making them turbulent, divergent, and filamented. Work on the Titan laser showed that artificially increasing the energy of the prepulse from 8 mJ to 1 J caused a significant reduction in the electron energy coupled into a cone-wire target [16,17]. This work indicated that the coupling efficiency into wire of the 1–3 MeV electrons of interest for heating applications such as FI decreased from 0.57% to 0.03%. However, it is not clear that decreasing the preplasma will indefinitely lead to higher coupling of laser light and electron acceleration. This is because, on the other extreme, a laser incident on a sharp solid-density interface should be reflected due to the high plasma frequency at solid density. Since on either extreme electron coupling into the solid target is low, there should exist an of optimal preplasma condition that will allow for the highest possible coupling of laser-to-electrons in the solid-target. Understanding the transition between these two regimes is important in order to optimize the generation of high-current energetic electron beams. This is especially important as state-of-the-art laser facilities (e.g., OMEGA EP [18], FIREX [19], NIF ARC [20]) invest heavily in upgrades to decrease prepulse in order to enhance the amount of electrons coupled into the solid targets.

In this article, we perform the first quantitative assessment of electron acceleration using experiments and simulations at a "high-contrast" laser facility where the on-target laser intensity is negligible until 80 ps prior to the peak of the pulse. Our work, demonstrated experimentally using Kα emission from cone-wire targets [21–24], shows that even this short 80 ps of laser interaction prior to the main pulse is enough to ablate a small amount of plasma ($1/e \sim 5$ μm) that is long enough to allow efficient electron acceleration, yet small enough that these electron are highly coupled into the solid-target. The physics of this interaction are elucidated using 2D Cartesian particle-in-cell (PIC) simulations that model the complete spatial and temporal evolution of the laser pulse. These simulations model the nonlinear interaction that accelerates electrons, which are recorded in time, space, and momentum. This fully constrains the electron source, which is injected into 2D cylindrical PIC simulations to match the geometry of the experiment. The simulations quantitatively reproduce the experimental data and indicate a laser to electron conversion efficiency of 32% $\pm$ 8% into all energies and 6.5% $\pm$ 2% into the 1–3 MeV energy range.

The experiments were performed on the Trident laser system at the Los Alamos National Laboratory [25]. This Nd:glass laser has a 1054-nm wavelength and a 580 $\pm$ 30 fs pulse length. Focusing with an f/8 parabola achieved a 13-μm full-width-at-half-maximum (FWHM) Gaussian-like spatial profile containing 40% of the laser energy. A maximum

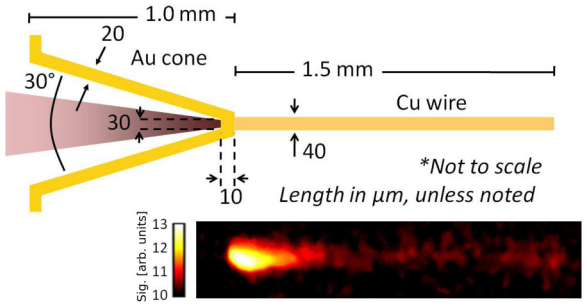

FIG. 1. (Color online) Top: Geometry of the cone-wire targets. Bottom: Pseudocolor image of Cu Kα x-ray emission from the wire.

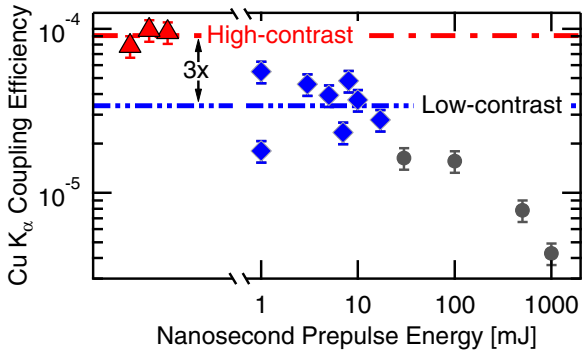

FIG. 2. (Color online) Experimental laser-to-Kα x-ray coupling efficiency from the high-contrast Trident laser (triangles) and the low-contrast Titan laser (diamonds/circles). Diamonds were taken with the intrinsic prepulse of the laser (1 to 17 mJ), while the circles [16] were taken with injected prepulse (up to 1 J). The double and triple dot-dashed lines are averages of the intrinsic prepulse cases.

energy of 75 J was delivered to produce 5×10^{19} W/cm^2 peak intensity. The temporal contrast of the laser was such that the laser intensity did not exceed 10^{11} W/cm^2 until 80 ps prior to the main pulse [25,26]. Additionally, experiments were performed at low-contrast using the Titan laser at Lawrence Livermore National Laboratory, which has similar laser characteristics (11-μm FWHM, 160 J, 650 fs) to Trident with the exception of having a prepulse containing 17 mJ in the 2.8 ns prior to the main pulse.

The targets used in our experiments consisted of a Au cone attached to a Cu wire as described in the caption of Fig. 1. This geometry allowed the accelerated electrons to be assessed by measuring the 8 keV Cu Kα x-rays created through collisions between the accelerated electrons and bound inner-shell electrons in the wire. The Cu Kα cross section is relatively constant for energies from 0.1 to 10 MeV [27] and thus provides a constraint on the number of electrons in this energy range. To constrain the electrons in both total energy and spectrum, both the total yield and spatial profile of the Kα emission were measured. The total yield was measured with a calibrated HOPG [28] spectrometer at 73° from the wire axis. The spatial image was taken using a spherical crystal imager [29] to reflect x-rays energies of 8048 eV with ~6 eV bandwidth placed at 71° from the wire axis. A sample image is shown in Fig. 1.

The opacity-corrected Kα coupling efficiency (Kα energy divided by laser energy) is plotted in Fig. 2 as a function of the laser prepulse energy. The circles show the decrease in coupling as prepulse is artificially increased up to 1 J energy as presented by Ma *et al.* [16] on Titan. The diamonds show data taken on Titan with variable intensity ($0.6–12 \times 10^{19}$ W/cm^2) by changing the laser energy with only the intrinsic laser prepulse (1–17 mJ). The triangles are shots taken on the Trident laser, which has a negligible prepulse (<1 μJ) that should not cause significant ablation in the nanosecond timescale. The Trident data indicates a ~3× increase in coupling efficiency versus the average intrinsic prepulse energy on Titan.

To understand the physics behind the increase in coupling efficiency, laser-plasma-interaction (LPI) simulations using the full-scale 2D spatial intensity profile and temporal profile of the Trident laser were performed. The LPI simulations were run using the direct-implicit particle-in-cell code LSP [30] in 2D Cartesian geometry. The simulation box included the solid-density Au cone and preplasma extending 40 μm from the inner cone tip, the 10-μm cone tip, and the first 95 μm of the Cu wire at solid-density. Boundary conditions allowed particles and fields to escape. The size of the box was 200 μm in the x direction and 185 μm in the z direction, which was large enough to avoid excessive charging along the boundaries. The resolution was 20 cells per laser wavelength and 133 time steps per laser cycle. Electrons and ions were initialized with 50 and 10 particles per cell, respectively. The Au was initialized with a charge-state of 10 and field ionization was included using the ADK model [31] with tabulated ionization energy tables [32]. The LPI simulations were run for 3 ps, which is enough time to simulate the full laser pulse and for the accelerated electrons to reach the inner cone tip. We note that our 2D simulations do not capture asymmetries in the azimuthal direction; however, previous work suggests that many such effects stem from having a finite angle between the laser and target surface [33], which is not the case in this study.

The major uncertainty in the Trident beam characteristics is the knowledge of preplasma generated prior to the arrival of the main pulse. While at longer timescales prepulse is negligible, the final 80 ps prior to the main pulse will have high enough intensity to ablate plasma from the target surface. Unfortunately, modeling of this ablation is difficult due to uncertainties of the material equation-of-state and of absorption at a sharp gradient over a short timescale, and measurement is difficult due to limited diagnostic resolution of small spatial scales. Thus, to bracket this uncertainty, and to investigate the role of varying preplasma, simulations were run varying the scale-length of an exponential profile from 0.1 to 5 μm. A final LPI simulation was run with a "low-contrast" preplasma profile as expected from the Titan laser system. This profile was prepared using the radiative hydrodynamic code HYDRA [34] with a prepulse energy of 17 mJ in 2.8 ns. The resulting preplasma profile is complex, but can roughly be fit with a 25-μm exponential scale-length.

Figure 3 shows the simulated number and energy densities of electrons near the peak of the pulse. In the lowest preplasma case, shown in Figs. 3(a) and 3(d), there is not enough low-density plasma to efficiently absorb the laser pulse. While there is still some electron acceleration near the cone tip, the amount of electron energy is much smaller. At the highest level of preplasma, shown in Figs. 3(c) and 3(f), there is a

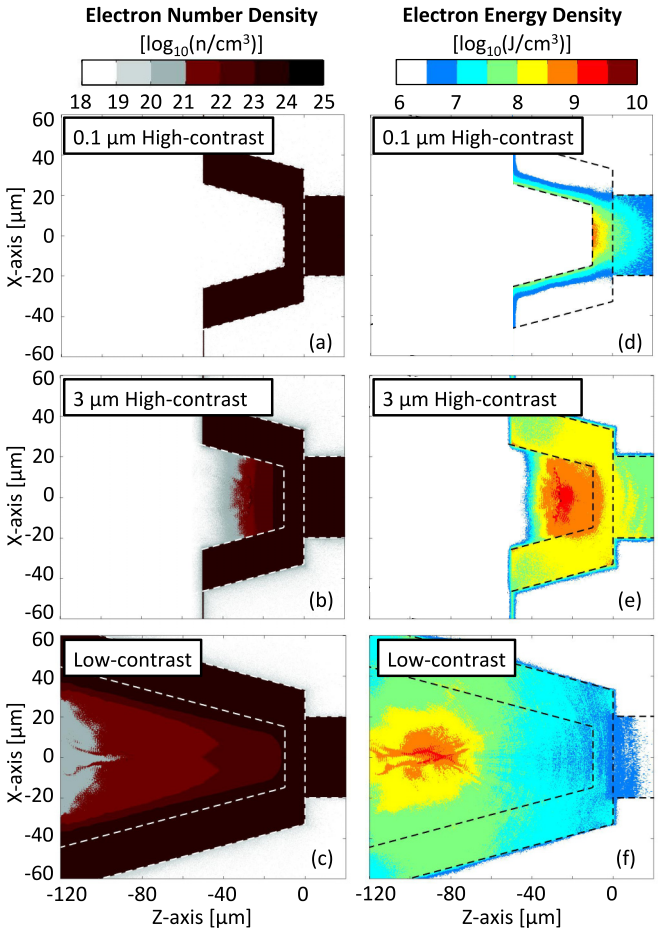

FIG. 3. (Color online) Electron number (a–c) and energy densities (d–f) from LPI simulations at 1 ps (near peak laser intensity), with dotted lines indicating the edges of the initial solid target. These simulations highlight the transition from a regime where little laser energy is coupling into the system (0.1 μm) into a case, into a regime of optimal coupling (3 μm), and finally into a regime where instabilities dominate the interaction (low contrast).

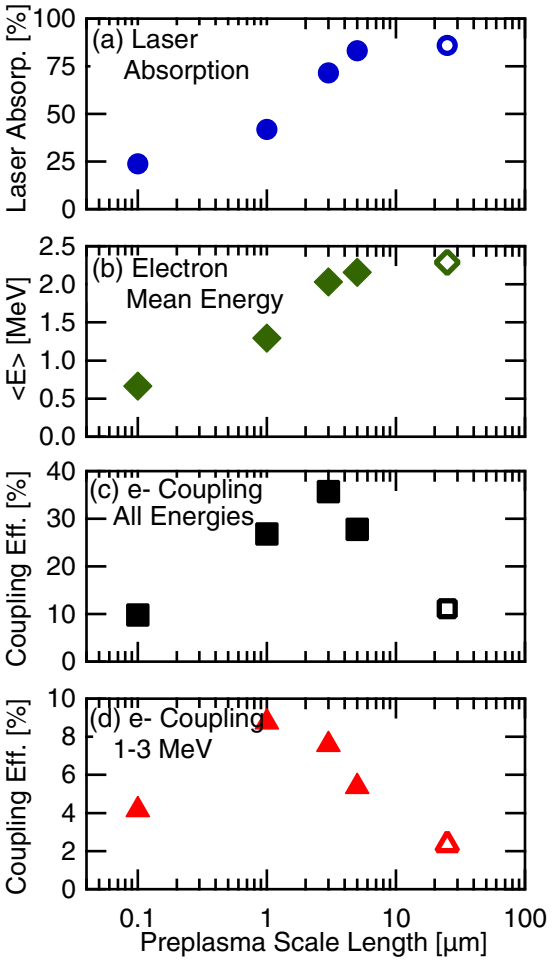

FIG. 4. (Color online) LPI simulations of the Trident laser pulse for varied preplasma scale lengths. (a) Laser energy absorption, (b) mean energy of the electrons coupled into the cone tip, and coupling of electrons into the cone tip integrated over (c) all energies and (d) from 1 to 3 MeV. Closed markers indicate an exponentially decaying plasma profile, while open markers show the longer low-contrast preplasma case simulated with HYDRA (17 mJ, ~25 μm).

large amount of low-density plasma where the laser is readily absorbed. However, this large amount of plasma leads to the filamentation and hole-boring of the laser that creates divergent and filamented electrons. Additionally, the electrons are far away from the cone tip, which decreases the solid angle and lowers their probability of coupling into the wire. Finally, in Figs. 3(b) and 3(e) we find a compromise between having enough low density to absorbing laser, but not having too little to seed strong instability growth. This case, which we will show later seems similar to the Trident laser, couples a high amount of energy into the electrons at a distance close to the tip of the cone.

As shown in Fig. 4, the laser absorption (incident minus reflected laser energy) increases dramatically with preplasma from 25% to 80% (solid circles) in the 0.1- to 5-μm cases and to 85% in the low-contrast case (open circle). This is due to a longer distance over which the laser can interact with and accelerate electrons, which also leads to an increase in the mean energy of the electrons [Fig. 4(b)]. Also shown is the coupling of electron energy passing through the inner tip of the Au cone, which has been rotated around the axis assuming azimuthal symmetry. Unlike the laser absorption, the coupling does not increase monotonically. Instead, the coupling into all electron energies [Fig. 4(c)] peaks at 35% in the 3-μm case, where the advantage of better laser absorption is overshadowed by the less-efficient coupling of these electrons into the cone tip. Of particular interest to FI and schemes where electron heating is important is the coupling of laser energy into electrons with energies between 1 and 3 MeV [Fig. 4(d)]. Interestingly, the peak coupling (9%) of these electrons is found at a smaller plasma scale length (1 μm) than for all electron energies, indicating that an longer preplasma predominantly enhances the acceleration of high-energy electrons, as opposed to low-energy electrons (as shown in Fig. 5). We note that there is a nearly 4× drop in coupling of the 1–3 MeV electrons in the low-contrast case compared to the peak at 1 μm. This is similar to the 3× drop in Kα conversion efficiency observed experimentally and is the reason that high-contrast leads to higher coupling.

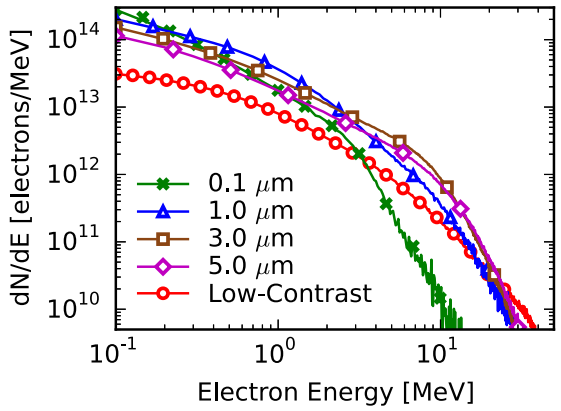

FIG. 5. (Color online) Electron spectra from LPI simulations. Plasma scale lengths of 0.1, 1, 3, and 5 μm and the low-contrast case are shown as lines with $\times$, $\bowtie$, $\square$, $\diamond$, and $\circ$ markers, respectively.

To quantitatively compare with the experimentally measured Kα emission profiles, the electrons from the LPI simulations crossing the inner-cone tip are recorded in time, space, and momentum. The energy spectra of these electrons are shown in Fig. 5. The electrons are passed to the inner cone tip of full-scale transport simulations also done using LSP, now in a 2D *cylindrical* geometry to correctly model the evolution of fields along the wire boundary, which would not be correct in 2D *Cartesian* geometry. The electrons undergo collisions treated through a test particle model [35] with the addition of radiative stopping [36] and Kα cross sections [27]. The background Au and Cu ions and electrons are modeled as fluid particles with an equation-of-state (EOS) from PROPACEOS [37,38] and temperature-dependent collision frequencies [39,40]. The cone extends backwards 300 μm from the tip and the 1.5-mm wire is completely included, both are modeled at solid density. Vacuum boundaries of 1 mm are extended from the edges of the target to ensure that the electric field development is completely modeled [41]. A single cell (1 μm) of protons at 2×10^{20} cm^{-3} is distributed along the edges of the cone and wire. These represent the hydrocarbon contaminant layer [42] found on most targets and are important because protons can accelerate more quickly than heavy ions and thus change the temporal development of the fields along the wire. A comparison of 1-μm and 100-nm cells for the proton layer was found to produce qualitatively similar results, with less than 20% difference in the effectiveness of proton acceleration.

The results of these simulations, after convolution with the imager spatial response, are shown in Fig. 6 compared to lineouts taken from the Kα imager discussed previously. The energy of the injected electrons comes from the LPI simulations as rotated around the axis assuming azimuthal symmetry. We note here that at high temperatures the peak energy of the Kα line emission can shift [43,44], which could cause some of the Kα emission to be out of the energy range of the imager diagnostic. However, according to the simulations, the temperature in the wire stayed below 30 eV, which is well below the value required to begin to shift the line of Kα energy out of the window of our imager diagnostic, which occurs around 50 eV [17]. This conclusion is supported by the consistency between the integrated emission from the imager and from the spectrometer.

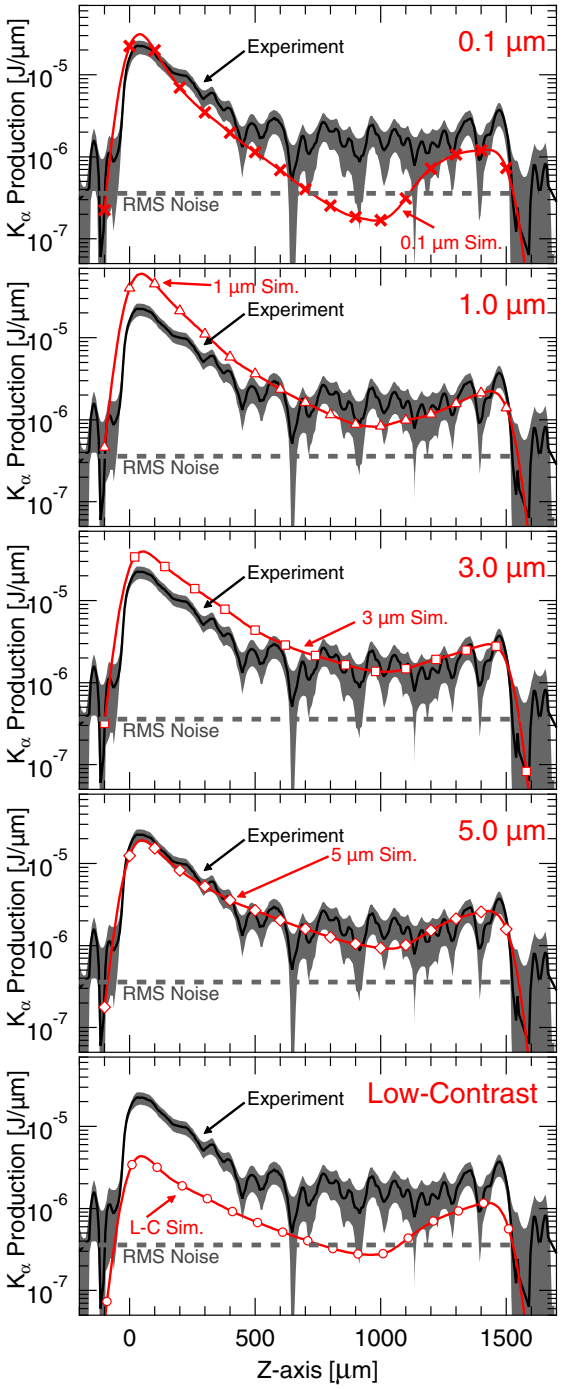

FIG. 6. (Color online) Cu Kα x-ray emission lineouts from the Cu wires. Experimental data (5×10^{19} W/cm^2) is shown as a solid line in all plots. The dotted line shows the root-mean-squared (RMS) noise level as calculated from regions of the image adjacent to the wire. The gray area surrounding experimental data indicates the uncertainty of data. Subplots show simulated data of 0.1-, 1-, 3-, and 5-μm scale lengths and the low-contrast (L-C) preplasma cases as lines with $\times$, $\bowtie$, $\square$, $\diamond$, and $\circ$ markers, respectively.

In general the simulated profiles peak at the beginning of the wire and then steadily decrease in signal until they rise again

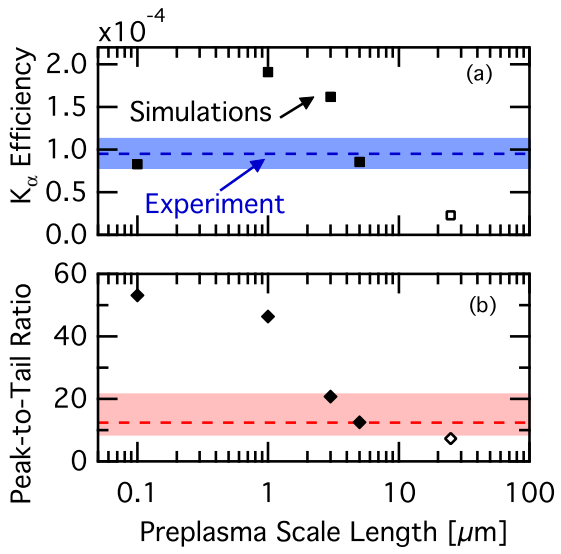

FIG. 7. (Color online) Markers show simulated (a) laser-to-Kα x-ray coupling efficiency and (b) peak-to-tail Kα ratio as a function of the preplasma scale length. The open markers show the low-contrast data. Experimental data is plotted as a dashed line with the uncertainty represented as a light area surrounding the line.

slightly at the end of the wire. This bump at the end of the wire is due to surfing electrons pushed by an interplay of electric and magnetic fields [17]. The electron distribution from the different preplasma cases causes significant differences in both the absolute amount of Kα emission and the shape of the profiles. We define two metrics from these profiles: (1) the laser-to-Kα coupling efficiency, which is simply the total Kα energy divided by the laser energy (74.5 J in all cases) and (2) the peak-to-tail Kα ratio, which we define as the maximum Kα signal divided by the average signal from the middle to the end of the wire (i.e., 0.75–1.5 mm). With these definitions we quantitatively compare the experimental to simulated data as shown in Fig. 7. For the laser-to-Kα coupling efficiency the experimental uncertainty is taken as the uncertainty in the Kα spectrometer. For the peak-to-tail Kα ratio the uncertainty is taken by using the largest range between the random uncertainty in the data.

One can see, either from the lineouts in Fig. 6 or the metrics in Fig. 7, that the coupling of Kα at first increases (i.e., from 0.1 to 1 μm) and then steadily decreases as the preplasma increases. This closely follows the coupling efficiency of the 1–3 MeV electrons showing how this diagnostic technique is sensitive to electrons of these energies. On the other hand, we find that the peak-to-tail ratio steadily decreases with the addition of more preplasma. This is due somewhat to the increase in the mean energy of the electron spectra with increasing preplasma, but also to the nonlinear interaction between the charging of the wire and the electrons surfing along the edges of the wire [17].

Of the simulations that we ran, the 5-μm case is the best fit to the experimental data. This is slightly unexpected, as the Trident laser is known to be a "high-contrast" laser. However, this suggests that this long level of preplasma is generated by the rising time of the laser ($\sim$80 ps). Thus, this rising time should not be neglected even when the nanosecond long prepulse is almost completely eliminated, as is the case of Trident. We can corroborate this using a simple estimate using an absorbed energy fraction from Ref. [45] and assuming that the preplasma number density n expands in time t and distance z with a self-similar profile [46] of $n(z,t) = \exp(-z/C_s t)$, where $C_s = \sqrt{TZ/m_i}$ is the sound speed at temperature T, ionization state Z, and ion mass m_i, as determined by the absorbed energy. Such an expansion yields a scale length of a few microns and thus is consistent with our simulations.

We find that only the 5-μm case simulation fits both the total Kα yield and the shape of the Kα profile (i.e., the peak-to-tail ratio). This consistency between the simulated and experimental data gives us confidence that our simulations are reproducing electron spectra that are realistic to the experiment. However, due to the finite uncertainty in the data, there should exist a range of scale lengths that would be within these error bars. Additionally, we expect the preplasma profile to be more complex than a simple exponential decay. Thus, in order to quantify the uncertainty in the electron coupling, we use the two best fitting simulations (i.e., 3 and 5 μm). We find that 28%–36% of the laser energy is coupled into electrons reaching the inner cone tip of all energies, based on the 5- and 3-μm cases, respectively, and a 5%–8% coupling efficiency into the 1–3 MeV energy range. Adding in quadrature the variation between these two simulations with the uncertainty in the spectrometer calibration gives an efficiency of $32\% \pm 8\%$ for all energies and $6.5\% \pm 2\%$ in to the 1–3 MeV range.

We note that this inferred value of coupling is significantly higher ($>10\times$) than previously reported work [16], which inferred of 0.57% coupling into 1–3 MeV electrons on Titan. This is partially due to the effect of preplasma, which our simulations show leads to a reduction of 2–3$\times$ in coupling. Additionally, it is due to a more complete physical model used in our recent work, which includes proton contaminants on the wire, electron angular divergence, and a LPI-simulated electron energy spectrum. And finally, the previous work defined the coupling efficiency as only the electrons within the wire (i.e., Au cone tip was not included). These higher coupling efficiencies, as well as recent work on the Omega laser facility [47,48], show a promising outlook for Fast Ignition research. Altogether, this large increase argues for continued effort into prepulse reduction in large laser systems to improve electron coupling.

In summary, we find that while very long scale lengths of preplasma are detrimental to electron coupling, the presence of a small scale-length preplasma ($1-5\,\mu$m) is necessary to achieve a high level of electron-coupling into the solid-target. However, even "high-contrast" lasers such as Trident often have enough energy in the <100 ps prior to the high-intensity peak to meet or exceed this optimal level. On the other hand, our work cautions against the idea that preplasma reduction is always an advantage. For instance, systems with shorter pulse lengths, lower intensities, or that are frequency doubled to eliminate prepulse may benefit from a slightly higher level of preplasma than they would naturally achieve.

The authors acknowledge the contributions of K. U. Akli, S. D. Baton, R. Fedosejevs, R. R. Freeman, H. Friesen,

S. Gaillard, D. Hey, G. E. Kemp, M. Koenig, A. G. Krygier, T. Ma, C. Murphy, D. T. Offerman, Y. Y. Tsui, D. Turnbull, T. L. D. Van Woerkom, B. Westover, T. Yabuuchi, and the Trident and Titan Laser team with performing the experiment. We are grateful for the work of D. W. Schumacher and C. Orban in the extended development and improvements to the LSP code. We acknowledge R.B. Stephens and E. Giraldez for fabrication and assembly of targets. This work performed under the auspices of the U.S. Department of Energy by Lawrence Livermore National Laboratory under Contract DE-AC52-07NA27344. D.P.H. was supported through the Lawrence Scholar Program at Lawrence Livermore National Laboratory.

[1] A. P. Fews, P. A. Norreys, F. N. Beg, A. R. Bell, A. E. Dangor, C. N. Danson, P. Lee, and S. J. Rose, Phys. Rev. Lett. **73**, 1801 (1994).
[2] R. A. Snavely *et al.*, Phys. Rev. Lett. **85**, 2945 (2000).
[3] S. Wilks *et al.*, Phys. Plasmas **8**, 542 (2001).
[4] J. Fuchs *et al.*, Nat. Phys. **2**, 48 (2005).
[5] B. S. Paradkar, T. Yabuuchi, H. Sawada, D. P. Higginson, A. Link, M. S. Wei, R. B. Stephens, S. I. Krasheninnikov, and F. N. Beg, Phys. Rev. E **86**, 056405 (2012).
[6] P. Patel, A. Mackinnon, M. Key, T. Cowan, M. Foord, M. Allen, D. Price, H. Ruhl, P. Springer, and R. Stephens, Phys. Rev. Lett. **91**, 125004 (2003).
[7] T. Ao, Y. Ping, K. Widmann, D. F. Price, E. Lee, H. Tam, P. T. Springer, and A. Ng, Phys. Rev. Lett. **96**, 055001 (2006).
[8] F. Perez *et al.*, Phys. Rev. Lett. **104**, 085001 (2010).
[9] H. Chen, S. C. Wilks, J. D. Bonlie, E. P. Liang, J. Myatt, D. F. Price, D. D. Meyerhofer, and P. Beiersdorfer, Phys. Rev. Lett. **102**, 105001 (2009); H. Chen *et al.*, *ibid.* **105**, 015003 (2010); **114**, 215001 (2015).
[10] C. P. J. Barty *et al.*, Nuclear Fusion **44**, S266 (2004).
[11] M. Tabak *et al.*, Phys. Plasmas **1**, 1626 (1994).
[12] S. C. Wilks, W. L. Kruer, M. Tabak, and A. B. Langdon, Phys. Rev. Lett. **69**, 1383 (1992).
[13] A. G. MacPhee *et al.*, Phys. Rev. Lett. **104**, 055002 (2010).
[14] A. J. Kemp, B. I. Cohen, and L. Divol, Phys. Plasmas **17**, 056702 (2010).
[15] T. Yabuuchi *et al.*, New J. Phys. **15**, 015020 (2013).
[16] T. Ma *et al.*, Phys. Rev. Lett. **108**, 115004 (2012).
[17] H. Sawada *et al.*, Phys. Plasmas **19**, 103108 (2012).
[18] J. Bromage, C. Dorrer, M. Millecchia, J. Bunkenburg, R. Jungquist, and J. D. Zuegel, AIP Conf. Proc. **1462**, 74 (2012).
[19] H. Shiraga *et al.*, Plasma Phys. Control. Fusion **53**, 124029 (2011).
[20] J. K. Crane *et al.*, J. Phys.: Conf. Ser. **244**, 032003 (2010).
[21] R. Kodama *et al.*, Nature **432**, 1005 (2004).
[22] J. Green *et al.*, Nat. Phys. **3**, 853 (2007).
[23] J. A. King *et al.*, Phys. Plasmas **16**, 020701 (2009).
[24] T. Ma *et al.*, Phys. Plasmas **16**, 112702 (2009).
[25] R. C. Shah *et al.*, Opt. Lett. **34**, 2273 (2009).
[26] S. Gaillard *et al.*, Phys. Plasmas **18**, 056710 (2011).
[27] C. Hombourger, J. Phys. B **31**, 3693 (1998).
[28] A. Pak *et al.*, Rev. Sci. Instrum. **75**, 3747 (2004).
[29] J. A. Koch *et al.*, Rev. Sci. Instrum. **74**, 2130 (2003).
[30] D. R. Welch *et al.*, Phys. Plasmas **13**, 063105 (2006).
[31] M. V. Ammosov, N. B. Delone, and V. P. Krainov, Sov. Phys. JETP **64**, 1191 (1986).
[32] T. A. Carlson *et al.*, At. Data Nucl. Data Tables **2**, 63 (1970).
[33] F. Pérez, A. J. Kemp, L. Divol, C. D. Chen, and P. K. Patel, Phys. Rev. Lett. **111**, 245001 (2013).
[34] M. M. Marinak *et al.*, Phys. Plasmas **8**, 2275 (2001).
[35] S. Atzeni, A. Schiavi, and J. R. Davies, Plasma Phys. Control. Fusion **51**, 015016 (2009).
[36] D. E. Groom and S. R. Klein, Eur. Phys. J. C **15**, 163 (2000).
[37] J. J. MacFarlane, I. E. Golovkin, and P. R. Woodruff, J. Quant. Spec. Rad. Transf. **99**, 381 (2006).
[38] J. J. MacFarlane, I. E. Golovkin, P. Wang, P. R. Woodruff, and N. A. Pereyra, High Energy Density Phys. **3**, 181 (2007).
[39] Y. T. Lee and R. M. More, Phys. Fluids **27**, 1273 (1984).
[40] M. P. Desjarlais, Contrib. Plasma Phys. **41**, 267 (2001).
[41] A. Link *et al.*, Phys. Plasmas **18**, 053107 (2011).
[42] M. Allen, P. K. Patel, A. Mackinnon, D. Price, S. Wilks, and E. Morse, Phys. Rev. Lett. **93**, 265004 (2004).
[43] G. Gregori *et al.*, Contrib. Plasma Phys. **45**, 284 (2005).
[44] P. M. Nilson *et al.*, Phys. Plasmas **18**, 042702 (2011).
[45] P. Mora, Phys. Fluids **25**, 1051 (1982).
[46] W. Kruer, *The Physics of Laser Plasma Interactions* (Westview Press, Boulder, CO, 2003).
[47] W. Theobald *et al.*, Nat. Commun. **5**, 5785 (2014).
[48] L. C. Jarrott, Bull. Am. Phys. Soc. **59** (2014).